INTERNATIONAL GEOLOGY REVIEW
https://doi.org/10.1080/00206814.2020.1734975

Taylor & Francis
Taylor & Francis Group

ARTICLE



# Disequilibrium crystallization and rapid crystal growth: a case study of orbicular granitoids of magmatic origin

Julin Zhang and Cin-Ty A. Lee

Department of Earth, Environmental and Planetary Sciences, Rice University, Houston, TX, USA

**ABSTRACT**

Archaean orbicular granitoids from western Australia were investigated to better understand crystal growth processes. The orbicules are dioritic to tonalitic spheroids dispersed in a granitic host magma. Most orbicules have at least two to three concentric bands composed of elongate and radially oriented hornblendes with interstitial plagioclase. Each band consists of a hornblende-rich outer layer and a plagioclase-rich inner layer. Doublet band thicknesses increase, crystal number density decreases, and grain size increases from rim to core, suggesting crystallization was more rapid on the rims than in the core. Despite these radial differences, mineral mode and bulk composition of each band are similar, indicating limited crystal-melt segregation during crystallization. These observations lead us to suggest that the orbicules represent slowly quenched blobs of hot dioritic to tonalitic liquids injected into a cooler granitic magma. The oscillatory bands in the orbicules can be explained by rapid, disequilibrium crystallization (supercooling). In particular, a linear correlation between bandwidth and radial distance from orbicule rim can be explained by transport-limited crystallization, wherein crystallization timescales are shorter than chemical diffusion timescales. The slope of this linear relationship corresponds to the square root of the ratio between effective chemical diffusivity in the growth medium and thermal diffusivity, resulting in effective chemical diffusivities of $3 \times 10^{-8}$ $m^2/s$. These high effective diffusivities require static diffusion through a free volatile phase (fluid) and/or a strong advective/convective component in the fluid. Regardless of the mechanisms, these effective diffusivities can be used to estimate growth rates of ~$10^{-6}$ m/s or 0.4 cm/hr. Our results indicate that crystals can grow rapidly, possibly facilitated by fluids and dynamic conditions. These rapid growth rates suggest that centimetre or larger crystals, such as in porphyritic and pegmatitic systems, can conceivably grow within days.

**ARTICLE HISTORY**
Received 16 December 2019
Accepted 23 February 2020

**KEYWORDS**
Orbicular granite; crystal growth; kinetics; diffusion; pegmatite

## Introduction

The abundances, sizes and shapes of crystals in magmatic systems reflect the thermal, compositional and dynamic evolution of magmas. Crystallization is the dominant control on magmatic differentiation, with crystal size and density partly controlling the efficiency of solid-melt segregation. Crystals may also influence volatile transport and generation of overpressures through their influence on bubble nucleation by providing nucleation surfaces within the magma (Hurwitz and Navon 1994; Klug and Cashman 1996; Sparks 2003). Finally, crystal abundance, shape and size can strongly influence magma rheology (Costa 2005).

Of interest here is quantifying how fast crystals can grow and what controls their growth rates in natural systems, but constraining growth rates in natural systems is challenging. Radioactive isotopes have been used in magmatic systems to estimate magma residence times (Vance and O'nions 1990; Christensen and DePaolo 1993; Reid *et al*. 1997), providing upper bounds on the rates of crystal growth (cm on timescales of 100 ky). Experimental studies, however, indicate that crystal growth can be rapid, on the order of cm/day or faster (Jahns and Wayne Burnham 1958; Lofgren 1974a, 1974b; Donaldson 1976; Swanson 1977), but the extent to which experimental conditions can be translated to natural systems is unclear. Rapid crystal growth (cm in <1 ky) has been suggested through modelling of trace element diffusion profiles in phenocrysts in rhyolitic systems (Gualda *et al*. 2012b; Shea *et al*. 2015a, 2015b), but whether such rapid growth rates operate in plutonic conditions is unclear.

Additional approaches are needed to quantify growth rates in nature. Diffusion modelling of trace element zonation, often assumed to be imparted by changes in composition or temperature of the magma, constrain crystal residence time and thus provide an indirect bound on crystal growth rate. More recently, zonation patterns have been suggested to be directly related to rapid crystal growth (Watson and Thomas 2009; Huang

**CONTACT** Cin-Ty A. Lee ctlee@rice.edu Department of Earth, Environmental and Planetary Sciences, Rice University, Houston, TX 77005, USA
Supplementary material for this article can be accessed here.

and Andreas 2012) rather than reflecting changes in external forcings (Ginibre *et al*. 2007; Druitt *et al*. 2012). If so, the trace element content of a crystal might potentially be used as a speedometer.

Here, we gain insight into crystal growth through a case study of magmatic orbicules. We use spatial variations in chemistry and textures to constrain crystal growth rates. These orbicules are ideal because they are shown to have formed by quenching of hot magmas injected into cooler magmas, allowing us to constrain crystallization times from thermal modelling. We use such constraints on cooling time to place bounds on crystal growth rates. We then explore the use of textural analyses as independent constraints on crystal growth rates.

## Geologic setting and samples

### *Geologic and petrologic description*

Six samples of orbicular granitoids were acquired from the Boogardie quarry at Mount Magnet in western Australia (−28.06116, 117.48503) (Figure 1). The orbicular granitoids come from a ~ 2.7 Gy old pluton and are concentrated in a 60 × 35 m oval-shaped body (Bevan and Bevan 2009; Fetherston 2010). The outcrop is composed of a felsic matrix, interspersed by spherical to oval-shaped mafic orbicules. The orbicules have diameters of ~8–12 cm and are slightly more mafic (dioritic to tonalitic) than the granitic host. Our samples represent individual orbicules that weathered out of the rock. The felsic host rock consists of quartz, plagioclase and biotite. The contact between the orbicules and the felsic matrix is generally sharp (Figure 1), but all orbicules display a thin biotite-rich rind separating the orbicule from the matrix (Figure 1). These biotite-rich rinds are reminiscent of those that mantle mafic enclaves (Farner *et al*. 2014) and are interpreted to represent reaction rinds. In many areas, the orbicules are abundant, packed so tightly that only a thin (~cm-scale) layer or septa of the host pluton separates adjacent orbicules. In some cases, orbicules are slightly flattened against neighbouring orbicules. Evidence for inter-penetration of orbicules or physical erosion of orbicule mantles is minimal. The above observations hint that the orbicules were emplaced into a viscous body, most likely a crystal-rich magmatic mush, undergoing ductile deformation. The orbicules themselves are characterized by a series of concentric bands, with each band consisting of a mafic (hornblende-rich) outer layer and felsic (plagioclase-rich) inner layer, which together are referred to here as a doublet (Figure 2). The repetition of doublets results in a black-and-white oscillatory pattern to the whole orbicule. The width of each doublet band increases towards the core (Figure 2).

We also analysed one Cretaceous orbicule (CA-1, Figure 2(g)) from the Green Acres gabbro (33.7, −117.1) complex in the Peninsular Ranges Batholith in southern California, USA (Berger 2014). These orbicules are part of a hornblende gabbro intrusive complex and occur as localized swarms along contacts between different batches of magmas. They resemble the Australian orbicules, but the thicknesses of the doublet bands are much thinner, resulting in finer and more numerous banding in the orbicules.

### *Petrographic and textural observations*

Orbicules were sliced down their mid-sections and polished. Each band is composed of radially oriented hornblende crystals separated by more equant plagioclase crystals (Figure 2). Grain boundaries between plagioclase and hornblendes are undulatory. The

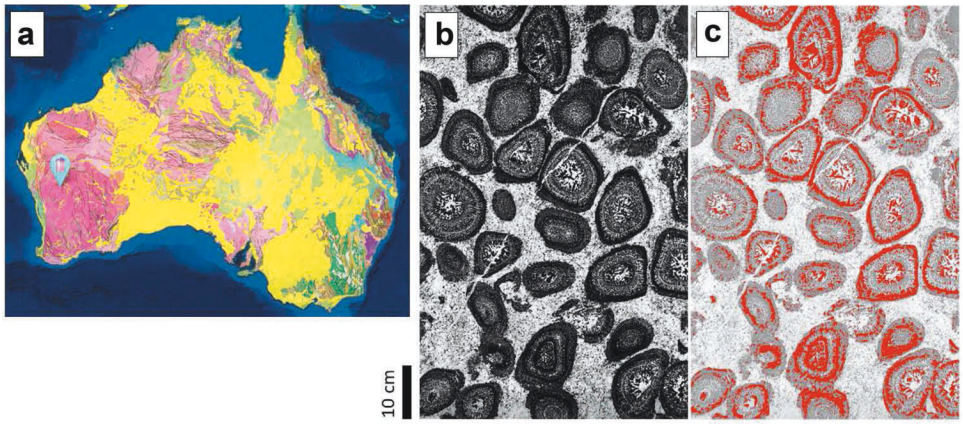


**Figure 1.** (a) Location of the Boogardie quarry as designated by the mineral icon. Geologic base map from Raymond *et al*. (2012); dark pink areas represent Archaean igneous and metamorphic basement. (b) Rock slab of orbicule swarm in felsic plutonic matrix. Note general lack of penetrative deformation between orbicules. Note also that each orbicule is surrounded by a fine-grained black biotite-rich rind. (c) Digitally enhanced version of (b) to highlight mafic rims and layers (red).

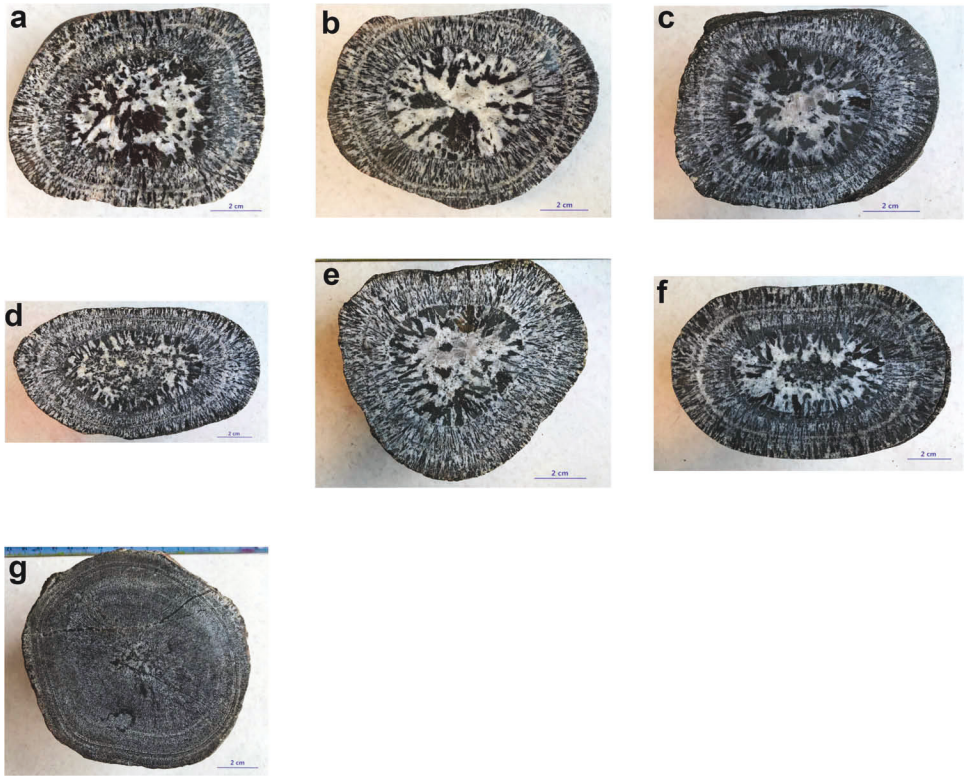


**Figure 2.** Photographs of six orbicular granitoid samples from western Australia (a-f) and one from California (g).

outward (towards the rim) pointing end of hornblende crystals tends to terminate at the same relative radial distance from the centre of the orbicule, while the inward (towards the core) pointing ends terminate at variable lengths and appear to taper inwards to a termination point. The uniform distance of outward termination gives rise to sharp outer boundaries for each doublet band. The outer part of each doublet is hornblende-rich, gradually becoming more plagioclase-rich inward within each doublet band. Doublet bandwidth increases inward as does average grain size within each band. We also see that grain number density decreases inward.

To better quantify some of these radially varying textures, samples were photographed and processed through ImageJ™ image processing software (data presented in Table 1). Hornblende area fraction in each band does not vary significantly from rim to core (Figure 3(a)), indicating that the bulk chemical composition in each band is homogenous from core to rim. Hornblende grain size, which we determine by shape analysis, increases from the rim of the orbicule to the core (Figure 3(b)). Number density (number of grains per unit area) of hornblende decreases from rim to core (Figure 3(c)). Doublet band width

**Table 1.** Textural data.

| | Radius (R) from rim (cm) | Band width (ΔR) (cm) | Hornblende Fraction (%) | Hornblende grain size ($mm^2$) | Number density ($n/cm^2$) |
|---|---|---|---|---|---|
| AUS-1 | 1.02 | 1.02 | 49.2 | 6.8 | 14.7 |
| | 2.11 | 1.09 | 54.4 | 9.4 | 10.7 |
| | 5.04 | 2.93 | 57.1 | 30.9 | 3.2 |
| AUS-2 | 1.28 | 1.28 | 49.3 | 5.4 | 9.1 |
| | 2.63 | 1.35 | 50.2 | 6.3 | 7.9 |
| | 5.78 | 3.15 | 39.3 | 17.5 | 2.2 |
| AUS-12 | 1.01 | 1.01 | 47.1 | 3.8 | 12.3 |
| | 2.06 | 1.05 | 45.5 | 4.0 | 11.5 |
| | 4.84 | 2.78 | 55.6 | 26.8 | 2.1 |
| AUS-15 | 1.52 | 1.52 | 47.9 | 4.7 | 10.1 |
| | 2.91 | 1.39 | 46.9 | 4.2 | 11.1 |
| | 6.87 | 3.96 | 54.1 | 33.4 | 1.6 |
| AUS-16 | 1.16 | 1.16 | 47.6 | 4.6 | 10.3 |
| | 2.25 | 1.09 | 37.4 | 2.1 | 17.7 |
| | 5.00 | 2.75 | 44.0 | 20.1 | 2.2 |
| AUS-17 | 1.22 | 1.22 | 62.7 | 11.6 | 5.4 |
| | 2.70 | 1.48 | 59.1 | 10.1 | 5.8 |
| | 6.20 | 3.50 | 51.7 | 23.7 | 2.2 |
| CA-1 | 0.09 | 0.09 | | | |
| | 0.15 | 0.06 | | | |
| | 0.26 | 0.11 | | | |
| | 0.40 | 0.14 | | | |
| | 0.62 | 0.22 | | | |
| | 1.36 | 0.74 | | | |
| | 1.53 | 0.17 | | | |
| | 2.55 | 1.02 | | | |
| | 3.26 | 0.71 | | | |
| | 4.24 | 0.98 | | | |
| | 5.50 | 1.26 | | | |

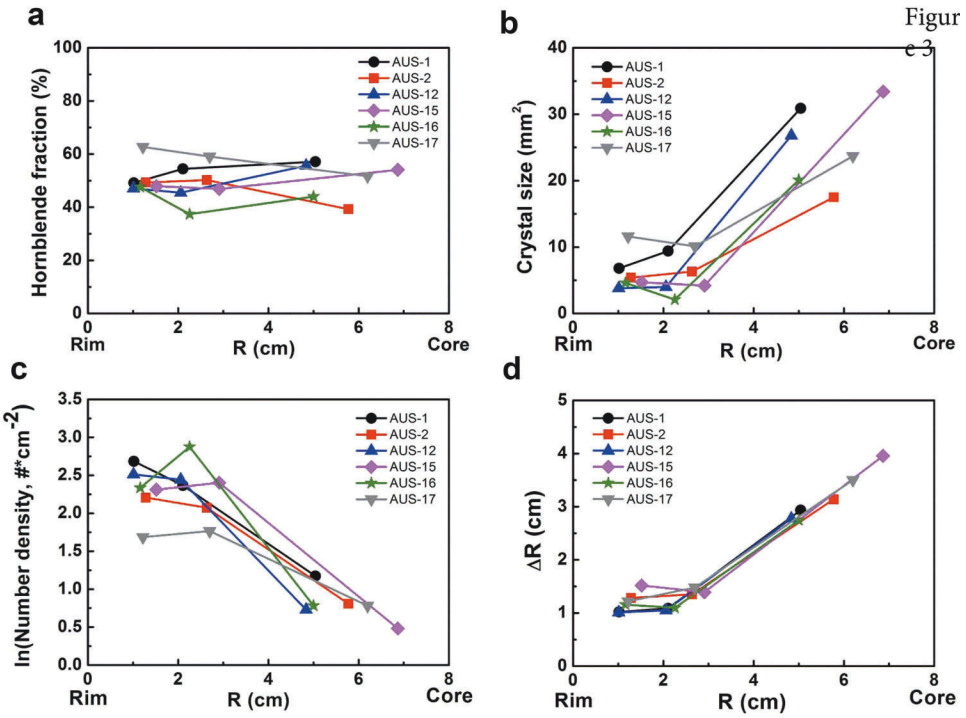


Figure 3. Results of image analysis for six orbicular granitoid samples from western Australia. Parameters are plotted versus radial distance from rim to core. (a) hornblende fraction in each orbicular band. (b) hornblende grain size in each band. (c) Natural logarithm of the number density of hornblende in each band. (d) Band width.

increases from the rim to the core (Figure 3(d)).

Samples were also scanned by micro-XRF to quantify their major elements (see Appendix). XRF elemental maps of a representative sample (AUS-1) are shown in Figure 4. Spatial variations in mineralogy, such as the mafic-felsic oscillatory banding, are also seen in the chemical maps, particularly for Fe and Ca. These XRF scanning results were further processed with ImageJ and converted to false colour maps for Fe and Al as shown in Figure 5. We then plotted intensities of various elements as a function of radius to better explore radial compositional variation. These transects were normalized to the bulk average so that they could be presented on the same scale (Figure 6). We see that Al, Fe, Mg, and Ca show oscillations associated with the doublet bands, but average elemental compositions remain constant from rim to core, that is, the bulk composition of each doublet is constant despite radial variation in grain size, grain number density and doublet band width (Figure 6). These observations are consistent with the above observation that bulk plagioclase-hornblende proportions in each doublet do not change from core to rim.

We also analysed the compositions of hornblendes in the different doublet bands. Major element maps from wavelength-dispersive electron probe microanalysis are shown in Figure 7 for sample AUS-1. It can be seen that average hornblende compositions do not change from orbicule core to rim. Zonation within individual hornblende grains is minimal. In summary, bulk doublet compositions and mineral compositions appear not to vary spatially within the orbicule.

## Interpretation of textures

Many hypotheses have been proposed to explain how orbicular granitoids form. We emphasize that rocks with orbicular textures almost certainly do not all form in the same manner. Some suggested processes include fractional crystallization of small melt bodies within the host magma, reactive nucleation on pre-existing xenoliths, mingling of two different kinds of magmas, metasomatism and liquid immiscibility (Moore and Lockwood 1973; Durant and Fowler 2002; Sylvester 2011; Smillie and Turnbull 2014; Ballhaus *et al*. 2015; McCarthy *et al*. 2016; McCarthy and Othmar 2017). Our goal is not to discuss all these different origins as our focus is on the particular suite of orbicules studied here. Evidence of ductile deformation of the orbicules indicates that the orbicules formed while both the host magma and the orbicules were still partially molten. The presence of biotite-rich rinds mantling the orbicules is similar to that seen in many magmatic mafic enclaves and undoubtedly reflects

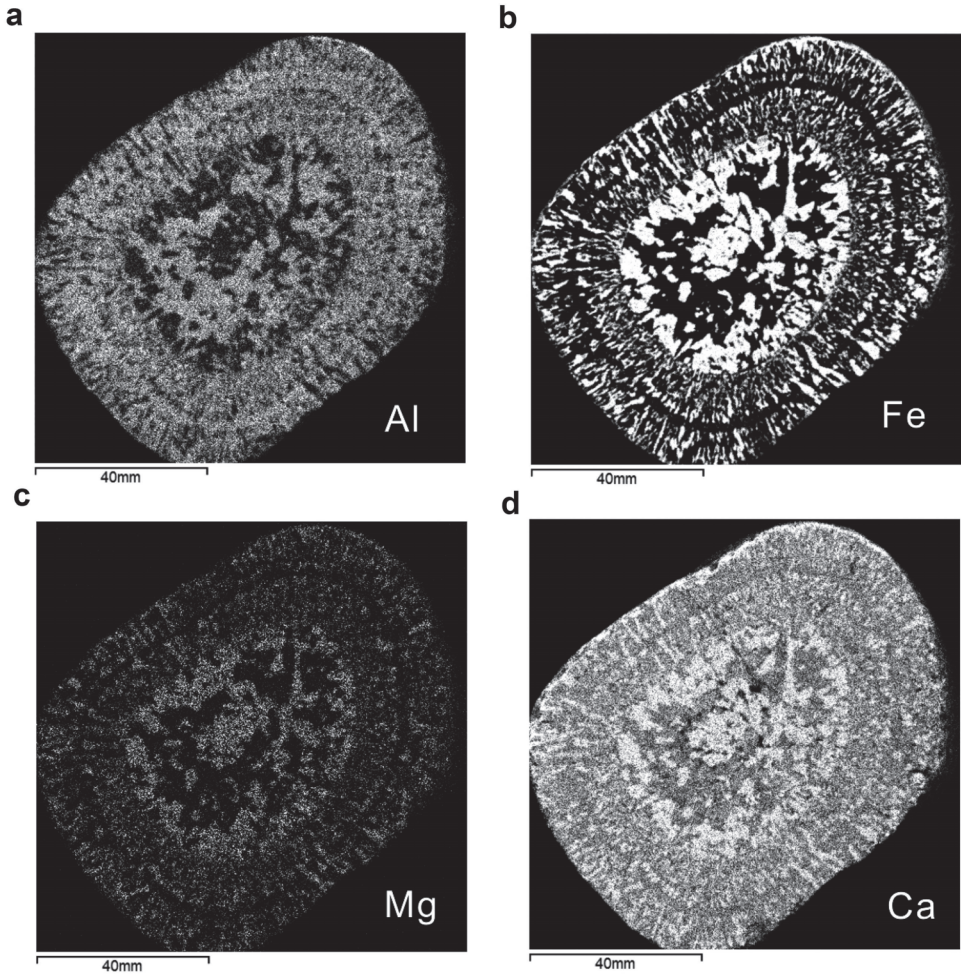


**Figure 4.** Micro-XRF elemental scans for sample AUS-1. (a) Al. (b) Fe. (c) Mg. (d) Ca (see Supplementary Table for data).

reaction between two lithologies not in thermal or chemical equilibrium (Farner *et al*. 2014). Thus, the presence of biotite-rich reaction rinds rules out strict liquid immiscibility as suggested by Ballhaus *et al*. (2015) because truly immiscible liquids would be in thermal and chemical equilibrium. Strict liquid immiscibility is also not supported by the radial variation in grain sizes.

The simplest explanation is that the orbicules initiated as hot, completely molten bodies, which then underwent rapid cooling and crystallization. The decrease in grain number density and the increase in grain size towards the core suggests high nucleation rates in the outer part of the orbicule and low nucleation rates in the core, the latter favouring crystal growth. This radial variation in nucleation density and grain size is not easily explained by reactive or metasomatic processes, but readily explained if the outer part of the orbicule cooled faster than the interior. The constant composition of each doublet also does not support a reactive or metasomatic origin.

We thus propose that these orbicules formed by the injection of a hotter magma (perhaps superheated) into a cooler magma, with the former in almost an entirely liquid state and the latter in a more crystal-rich state. The textures are best explained as a result of quenching. The lack of radial variation in doublet composition suggests that crystallization occurred at rates faster than liquids could segregate from the crystals. Exactly how these hot magmas were injected is not important for this paper, but whatever the cause, the conditions for injection must have been local given the limited occurrence of these orbicule swarms to local outcrops. In any case, if the orbicules were originally hot, it is not difficult to envision scenarios in which hot, molten liquids were introduced into the granitic host through Rayleigh–Taylor type instabilities developed between two different magma bodies. One possible scenario for such an origin could be the underplating of a hot magma against a cooler

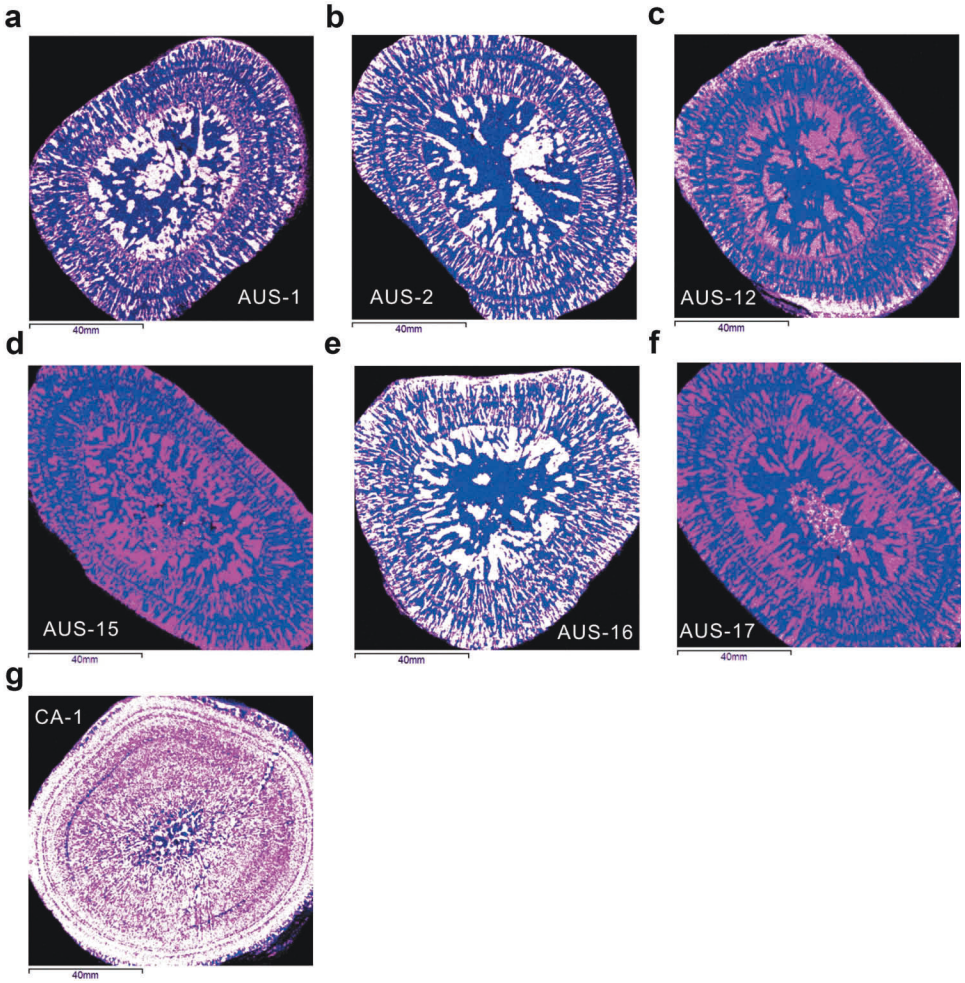


**Figure 5.** False colour images for six Australia samples and one California sample. Fe is denoted by white to pink colour while blue represents Al. (a) AUS-1. (b) AUS-2. (c) AUS-12. (d) AUS-15. (e) AUS-16. (f) AUS-17. (g) CA-1.

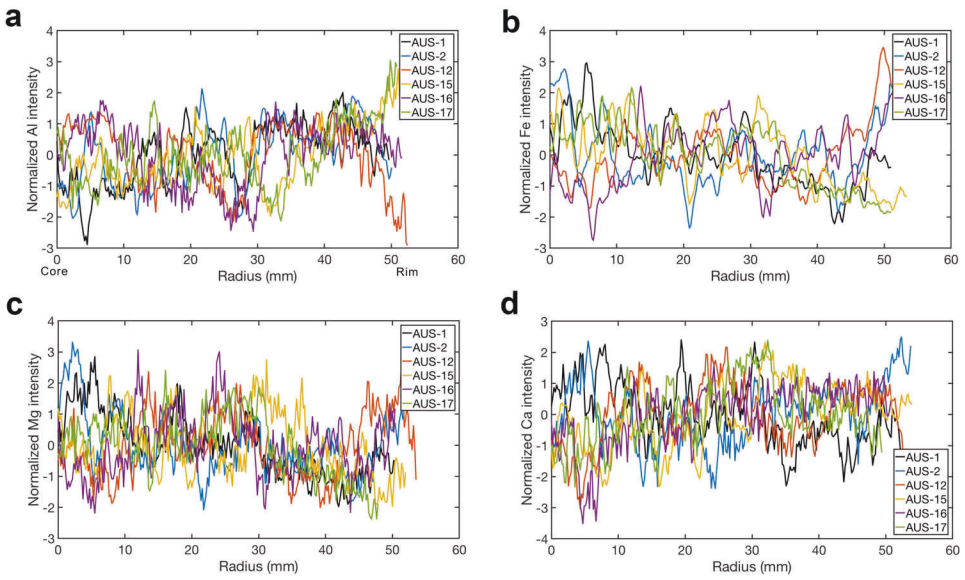


**Figure 6.** Transects of intensities of major elements as a function of radius for all Australian orbicule samples. Each transect was normalized to the average intensity of every element of each sample. (a) Al. (b) Fe. (c) Mg. (d) Ca.

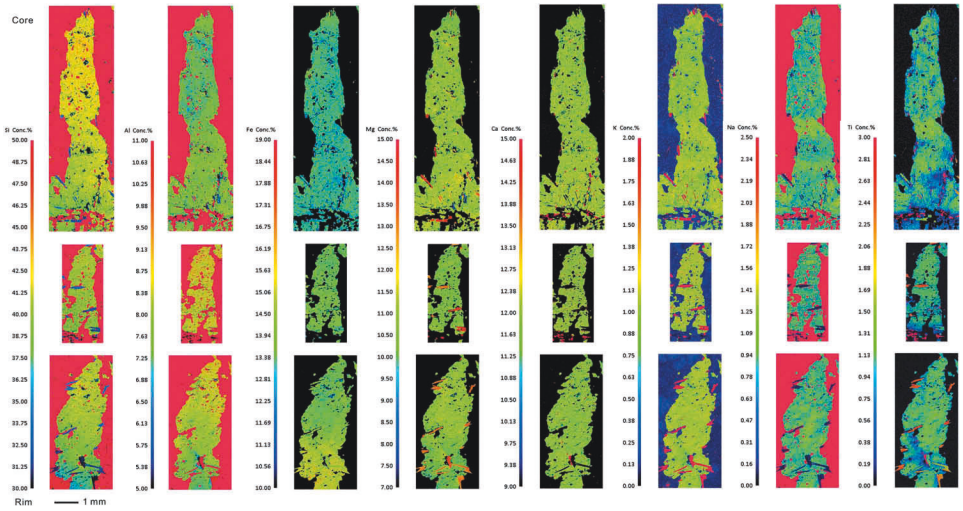


**Figure 7.** Wave-length dispersive electron probe microanalytical elemental maps of hornblendes in different sections of an orbicule (AUS-1). Bottom to top represents outer (rim) part of orbicule to central (core) part of orbicule (up direction points towards core). Note there are no obvious changes in composition of hornblendes from orbicule rim to core.

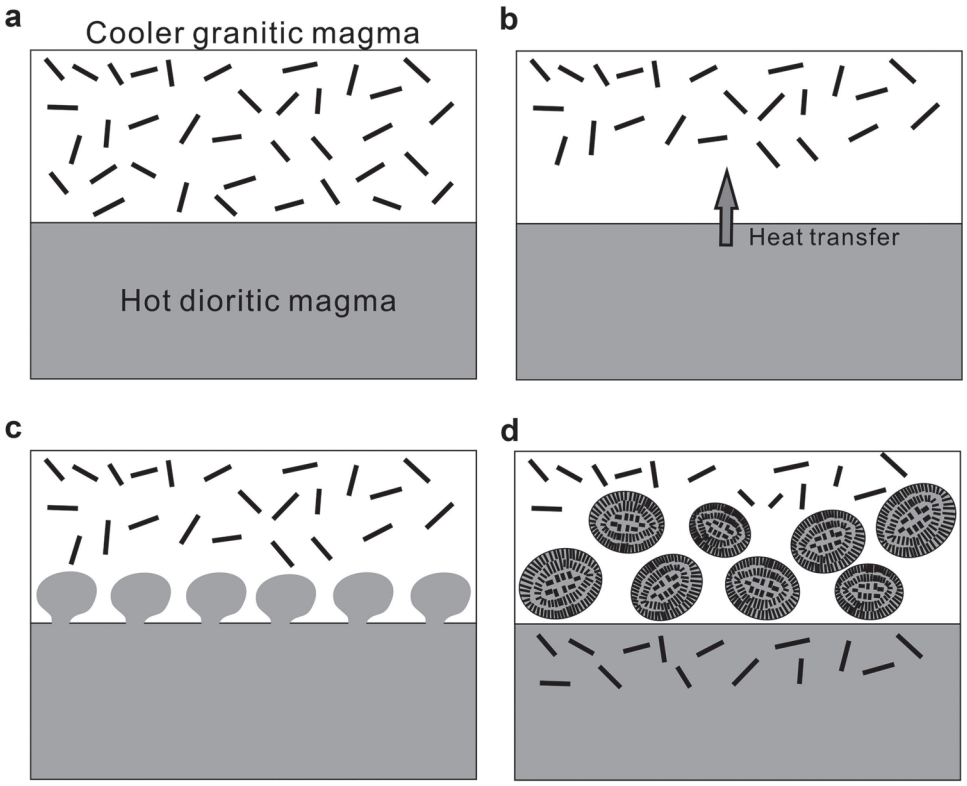


**Figure 8.** A series of cartoons showing how orbicular granitoids from western Australia may have formed. (a) First, a hot dioritic magma underplates and heats a cooler granitic magma. (b) Heating melts the crystals at the bottom of the cooler granitic magma, reducing the crystallinity and viscosity of the bottom of the granitic magma body. (c) This then allows the dioritic magma to be injected into the cooler granitic magma in the form of blobs. (d) The dioritic blobs cool and solidify to form the orbicules with concentric bands.

magma body (Figure 8). This juxtaposition could result in basal heating of the cooler magma body, reducing its crystallinity and viscosity, which would then allow hotter liquids from below to locally rise into the heated base of the over-riding magma body. Our proposed origin is consistent with the

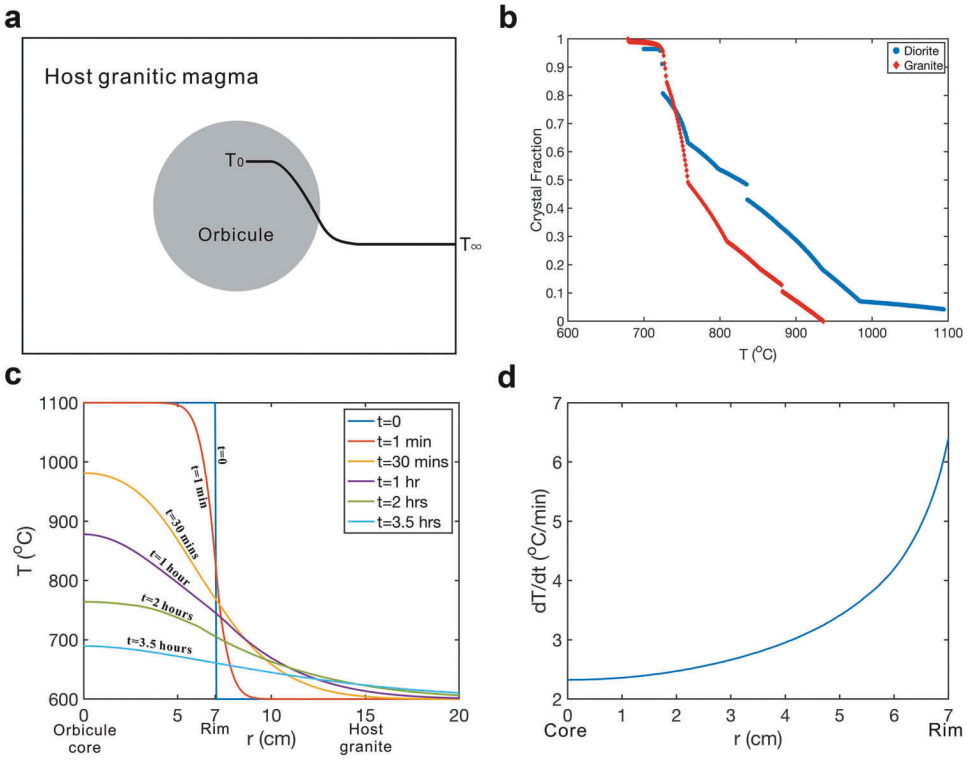


**Figure 9.** Temperature profiles across the boundary between a hot dioritic orbicule and the cooler host granitic magma. (a) cartoon. (b) The relationship between crystal fraction and temperature for the dioritic and granitic magmas as calculated from MELTS (assuming 4 wt. % bulk $H_2O$). (c) The thermal diffusion model results show that the temperature profiles change with elapsed time. Initial temperature of the dioritic magma is 1100°C and 600°C for the host granite. (d) The average cooling rate profile within the orbicule where r = 0 denotes the orbicule core and r = 7 cm for the rim.

interpretation of Bevan and Bevan (2009) and Fetherston (2010) for the same rocks.

Given this hypothesized origin by mafic injection, the question arises as to why these radial textures are not commonly found in the ubiquitous mafic enclaves found in many plutonic systems as such enclaves are widely thought to represent evidence of mafic-felsic magma mixing. We note that where mafic and felsic magmas indeed mingle, quench rinds on the mafic lithologies are seen (Wiebe 1994), in many cases leading to dendritic crystal growth and oscillatory layering (e.g. comb layering). However, the majority of mafic enclaves do not show such features because most mafic enclaves represent already solidified rock fragments when they were entrained into felsic magmas, and thus do not represent bonafide liquid-liquid mingling. In fact, most mafic enclaves are angular (Farner *et al*. 2014) and many of the reported quench rinds seen on enclaves are actually reaction rinds (Liao *et al*. 2013; Farner *et al*. 2014).

## Quantifying crystal growth rates

### *Cooling timescales*

We assume that the time allowed for crystals to grow cannot exceed the elapsed time for melt to completely solidify. A maximum constraint on the crystal growth time and a minimum constraint on crystal growth rate can thus be derived from the solidification time of a melt. We modelled the cooling of the spherical blobs through conductive cooling to obtain the solidification time of an initially crystal-free dioritic melt (Figure 9(a)). If the melt or fluid in the blob were undergoing thermal convection, growth times would be even shorter and growth rates faster. We used a thermal conduction equation with latent heat, where $T$ is temperature, $t$ is time, and $r$ is radial distance from the core (following Lee *et al*. 2015):

$$\frac{\partial T}{\partial t} = \frac{1}{r^2}\frac{\partial}{\partial r}\left(r^2\frac{\partial T}{\partial r}\right) + \frac{L}{C_p}\frac{dF}{dT}\frac{\partial T}{\partial t} \quad (1)$$

$$T(t = 0, r \le R^*) = T_o$$

$$T(t = 0, r > R^*) = T_\infty$$

$$\frac{\partial T}{\partial r}(r = 0) = 0$$

In the above, $R^*$ is the radius of the spherical orbicule (~7 cm), $C_p$ is specific heat capacity ($1.0 \times 10^3$ J/(kg K) for diorite and $0.95 \times 10^3$ J/(kg K) for granite (Somerton

1992)), $\kappa$ is thermal diffusivity ($4.5 \times 10^{-7}$ $m^2/s$ for both diorite and granite at 600–1000°C (Hartlieb *et al*. 2016)), $L$ is the total latent heat of crystallization ($4 \times 10^5$ J/kg for both diorite and granite (Lange *et al*. 1994)), $F$ is crystal mass fraction, and $dF/dT$ is a measure of how $F$ varies with temperature. Specific heat capacity, thermal diffusivity and latent heat of crystallization are all assumed to be constant. The term on the left side of Equation (1) describes the temperature change of the magma as a function of time and space. The first term on the right represents the transfer of heat via conduction and the second term represents a heat source through the release (or absorption) of latent heat of crystallization (or melting). The term $dF/dT$ in the latent heat term was parameterized using Rhyolite MELTS (Gualda *et al*. 2012a; Ghiorso and Gualda 2015) for the generalized dioritic and granitic bulk compositions (see Appendix). We assumed a homogeneous initial temperature $T_0$ of 1100°C for the hot dioritic melt and a time-constant far field temperature in the granitic host $T_\infty$ of 600°C (infinite half-space approximation). Based on our parameterization of $F(T)$, we find that a cooling of ~350°C below the liquidus results in approximately 70–80% crystallization (see also Lee *et al*. (2015)) (Figure 9(b)). This crystal fraction is above the critical fraction at which mineral grains begin to form an interlocking framework (Moitra and Gonnermann 2015), so we take 750°C to represent the temperature at which unimpeded crystal growth effectively terminates.

Equation (1) is solved numerically (see Appendix) and our results are shown in Figure 9(c). This thermal model allows us to calculate average cooling rates as a function of radius. We can estimate average cooling rate $dT/dt$ at a given radius by dividing the temperature difference between initial temperature (1100°C) and the temperature of solidification (750°C) by the average time to cool through that temperature interval. These modelled cooling rates are plotted as a function of radius in Figure 9(d), where it can be seen that cooling rates are, of course, faster on the rims. The core of the orbicules solidifies within ~2.5 h, corresponding to an average cooling rate of ~2.3°C/min (Figure 9(d)). However, cooling rates are much faster on the rims, such that the rims fully crystallize in <1 hr, corresponding to an average cooling rate of ~6.4°C/min (Figure 9(d)). Given average crystal lengths on the rim of ~6 mm, this suggests crystal growth rates of ~$1.8 \times 10^{-6}$ m/s (0.65 cm/hr) at the rim. Similar calculations done on the core crystals yield growth rates of ~$1.1 \times 10^{-6}$ m/s (0.40 cm/hr) for 10 mm long crystals in the core, a factor of ~1.5 slower than on the rims.

We note that our thermal models assume that the far-field temperature $T_\infty$ of the granitic host does not change with time, which implicitly assumes that the host pluton does not cool off during the formation of the orbicule or that it does not heat up from the cumulative addition of hot orbicules. The former assumption is reasonable because we assume that pluton cooling timescales (kys) are much longer than orbicule entrainment and quenching timescales (hours). The latter assumption is valid only if orbicules, at the time of their cooling, are sufficiently far enough from each other that they do not influence the thermal evolution of their nearest neighbours. The minimum distance between orbicules for our model to be valid is the thermal conduction length scale, which would be approximately 1–2 orbicule diameters, suggesting that our infinite half-space assumption is clearly an approximation given the slightly smaller separation distances observed. Our cooling times may thus be underestimated and our crystal growth rates over-estimated based on thermal modelling alone, although it is also possible that the orbicules were more widely spaced before they accumulated. If any convective component existed in the orbicule, our calculated timescales are upper bounds and crystal growth rates minimum bounds.

## Nucleation rate versus radius

Our thermal models allow us to use effective average cooling rates to compare to our estimates of nucleation density. In Figure 10(a), we plot the natural log of nucleation density versus modelled cooling rate, yielding a curved positive correlation. This positive correlation between nucleation rate and cooling rate is consistent with nucleation theory, corroborating our suggestion that these orbicules cooled inward from the rim into the core. Further insight can be had by plotting nucleation density versus degree of undercooling. By multiplying average cooling rate $dT/dt$ (as in Figure 9(d)) by the total time for crystallization of the orbicule, we can also plot effective undercooling as a function of radius (Figure 10(b)). This, in turn, allows us to plot nucleation density versus undercooling degree and compare to the empirical relationship describing nucleation rate ($I$) versus the average degree of undercooling

$$\ln(I) = -\frac{A}{T\Delta T^2} - \frac{B}{T} + C \tag{2}$$

where $T$ is the average effective temperature of the system at radius $r$, $\Delta T$ is the average undercooling given by $\Delta T = T_L - T$, where $T_L$ is the liquidus of the melt, and $A$, $B$ and $C$ are constants (Neilson and Weinberg 1979; Lasaga 2014). To use Equation (2), we can obtain a time-averaged nucleation rate $I$ by dividing nucleation density $N$ by the average time for cooling, which increases towards the core. In Figure 10(c), it can be seen that the natural logarithm of nucleation density correlates negatively with the inverse of the square of

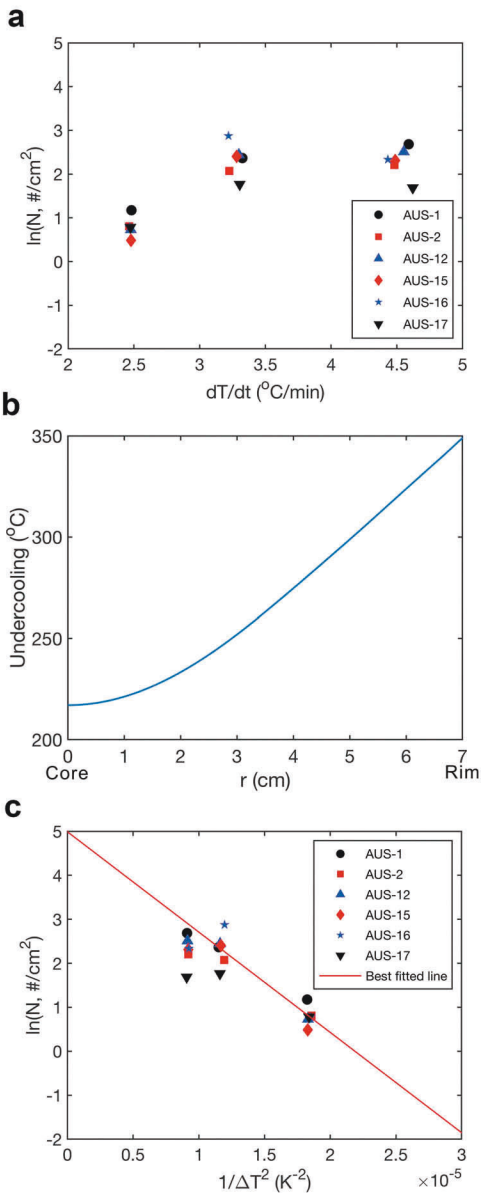


**Figure 10.** (a) Positive correlation between natural log of nucleation density and cooling rate. Each symbol type represents a different orbicule. (b) An example of undercooling degree versus radius from core to rim at time t = 1 h. Undercooling degree is higher at the rim than at the core. (c) Natural log of nucleation density versus the inverse of the square of undercooling. Straight red line is a least-squares fit through the low undercooling data. When undercooling rates are high (rim), the data deviate from the linear relationship with $1/\Delta T^2$.

undercooling degree ($1/\Delta T^2$), which is consistent with theory if $T$ in Equation (2) is approximately constant as should be the case if undercooling is small. For large undercoolings (rim), a deviation from this theoretical relationship can be seen both in the data (Figure 10(c)). In any case, the observed spatial distribution of nucleation density is consistent with our hypothesis that orbicules formed by rapid cooling of hot blobs of magma emplaced into a cooler host magma.

## *Kinetic controls on formation of oscillatory banding*

As discussed above, the most distinctive feature of the orbicules is the series of mafic-felsic doublet bands, with doublet band thickness increasing towards the core. We hypothesize that the thickness of each doublet band is controlled by the flux of growth nutrients to the crystal, which, in turn, is limited by diffusional transport of nutrients in the growth medium (magma). If the rate of crystal growth is limited by the diffusional supply of 'nutrients',

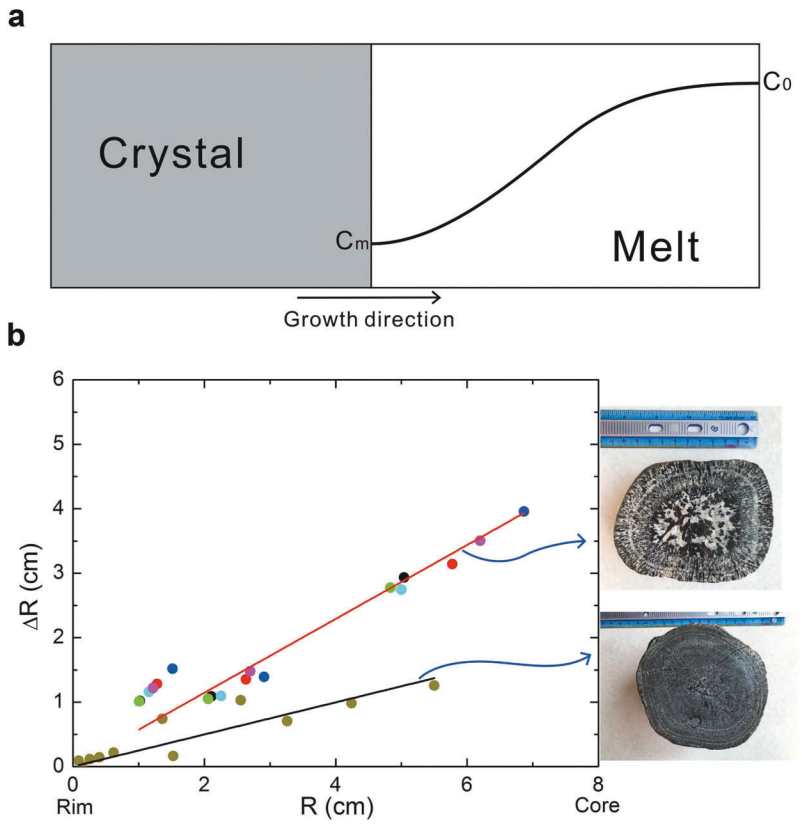


**Figure 11.** (a) A cartoon showing how crystal growth is controlled by the flux of nutrient from the growth medium (melt) to the crystal. $C_o$ represents far-field concentration in melt and $C_m$ represents concentration in melt at the advancing crystal-melt interface. (b) Bandwidth versus inward radius *R* of the orbicule. The olive green circles represent the California sample while all others represent western Australia samples.

then rapid crystal growth will lead to a nutrient-depleted chemical boundary layer in the growth medium ahead of the advancing crystal front (Figure 11(a)). This nutrient-depleted boundary develops if crystal growth rates are comparable or faster than the diffusive flux of the nutrients in the magma back towards the crystal. At steady state and in one dimension, crystal growth rate $dx_c/dt$ relates to the diffusive flux as follows (Lewis *et al.* 2015)

$$\rho_x \frac{dx_c}{dt} = D\rho_m \frac{dC_m}{dx_m} \tag{3}$$

where $\rho_x$ and $\rho_m$ are the densities of the crystal and melt, *D* is the effective chemical diffusivity of the rate-limiting nutrient in the growth medium *m*, $C_m$ is the mass concentration of the rate-limiting nutrient in the growth medium and $dC_m/dx_m$ is the compositional gradient in the growth medium at the crystal-melt boundary. At steady state, this gradient is approximated by dividing the compositional difference $\Delta C_m$ across the chemical boundary layer by the thickness of the chemical boundary layer $\Delta x_m$. The chemical boundary layer thickness depends on the chemical diffusivity (*D*) of the nutrients and scales with time as $\sqrt{D\tau}$, where $\tau$ represents the elapsed time for crystal growth. This elapsed time corresponds to the average crystallization time because after the system has cooled below the solidus, crystallization is complete and chemical diffusion is effectively arrested. Thus, for rapid cooling, there is insufficient time to transport far-field nutrients to the growing crystal, quickly terminating crystal growth and resulting in narrow bands. The elapsed time$\tau$ for crystals to grow is the thermal diffusion timescale, which must scale with the radial distance from the rim of the orbicule, *R*, to the doublet, that is, $\tau \approx R^2/\kappa$. By non-dimensionalizing the chemical diffusion equation using the thermal diffusion timescale as the characteristic time (and ignoring the small effect of latent heat), the following scaling between the thickness of each doublet and the radial distance of the doublet from the margin is

$$\frac{\Delta R}{R} \sim \sqrt{\frac{D}{\kappa}} \tag{4}$$

This scaling indicates that the thickness of the doublet band should correlate linearly with radial distance from rim, increasing in thickness towards the core. Most importantly, the slope of the line is given by $\sqrt{D/\kappa}$,

which means that if thermal diffusivity $\kappa$ is known, then the effective chemical diffusivity of the rate-limiting nutrient is known. In Figure 11(b), we show that our observed $\Delta R$ scales linearly with $R$ in both the Australia and California orbicules, consistent with our hypothesis for orbicule growth through quenching.

Linear regression of $\Delta R$ versus inward radius $R$ yields a slope of ~0.57 for the Australian orbicules and ~0.25 for the California sample (Figure 11(b)). For a thermal diffusivity of ~$10^{-7}$ $m^2/s$ for silicate melts at ~1000°C (Eriksson *et al*. 2003), this slope yields an effective chemical diffusivity of ~$3 \times 10^{-8}$ $m^2/s$ for the Australian samples and ~$6 \times 10^{-9}$ $m^2/s$ for the California sample. Because these are effective chemical diffusivities, we do not know which element this chemical diffusivity corresponds to. We assume that this effective diffusivity represents that of the molecular species needed to make hornblende. In this regard, we note that chemical diffusivities of various cations in silicate melts, such as a dioritic melt, are on the order of $10^{-12}$ – $10^{-11}$ $m^2/s$ (Baker and Hélène 1994), far slower than that inferred here. This large difference between our estimate of effective chemical diffusivities and that from experimental constraints may imply our crystal growth models are wrong. However, our independent constraints on growth rates are reasonable given the short (hours) thermal lifespan of the orbicule as described above.

One way to reconcile the high effective chemical diffusivities inferred here is if there is an advective component in the growth medium (melt or fluid) in addition to chemical diffusion. For example, we have not considered the possibility of internal convection within the orbicule. With advection, the width of the diffusive boundary layer would be substantially reduced, giving rise to steep chemical gradients that would drive more rapid crystal growth. Reduction of the width of the diffusive boundary layer would be manifested as high effective chemical diffusivities.

Another possibility is if the diffusivities reflect transport through an aqueous fluid rather than a silicate melt. If the orbicule had saturated in water during crystallization, a free fluid phase would be released. If the free fluid phase were interconnected, a fast diffusion pathway would be generated and the diffusivity of interest would be through the fluid phase, not the silicate melt. Chemical diffusivities through water are much faster than through silicate melt. For example, the chemical diffusivity of Mg in water at 25°C is $7.05 \times 10^{-10}$ $m^2/s$ (Li and Gregory 1974), but at 800°C is $5.8 \times 10^{-8}$ $m^2/s$, approaching that determined in this study (extrapolated using the method in Nigrini (1970)). The factor of five lower effective diffusivities calculated for the California sample compared to the Australian samples is noteworthy. Given the more mafic composition of the orbicule and host pluton in the California samples, we speculate that the California samples would have had less free water available, resulting in a smaller fraction of interconnected free fluid pathways and thus a smaller effective diffusivity. In any case, such high effective diffusivities are not unreasonable as apparent diffusivities for alkalis in aqueous fluids can be as high as $10^{-8}$ $m^2/s$ as constrained experimentally by Morgan *et al*. (2008).

## Estimating rates of crystal growth

We conclude that these high effective diffusivities likely reflect the combination of the presence of a free fluid phase and internal advection within the orbicule. Regardless of what generates these high effective diffusivities, we can still use these values to estimate crystal growth. Fast effective diffusion through fluids would enhance the efficiency by which nutrients are transported in the growth media to the growing crystals. Assuming crystal growth is limited by diffusive transport through a boundary layer, we can approximate crystal growth rates from the following equation (identical to Equation (3) except density terms have been dropped)

$$\frac{dx_c}{dt} \sim D\frac{\Delta C_m}{\Delta x_m} \tag{5}$$

where $\Delta x_m$ is the width of the chemical boundary layer in the melt ahead of the advancing crystallizing front. This equation is valid even with fluid advection; advection serves to thin the boundary layer. We take $\Delta x_m$ to approximately equal the width of each orbicule doublet band ($\Delta x_m \sim \Delta R$) and $\Delta C_m$ to be the extent of supersaturation across the boundary layer. To solve for $\Delta C_m$ in Equation (5), we assume a binary system with only two endmembers: hornblende and plagioclase. For steady-state crystal growth, we can assume that the melt is saturated and in equilibrium with hornblende at the crystal-melt interface whereas the far-field melt is supersaturated in hornblende with a bulk composition defined by the hornblende component in the initial magma itself. Therefore, $\Delta C_m$ denotes the difference between bulk composition and the composition at hornblende saturation in the melt. The hornblende saturation composition in the melt decreases with decreasing temperature so $\Delta C_m$ increases as temperature decreases.

The above concept is illustrated in a binary phase diagram where temperature is plotted as a function of composition $X$, with plagioclase and hornblende serving as endmembers (Figure 12(a)). The top diagonal lines represent liquidus lines. The horizontal line represents the solidus, below which the system is solid. The

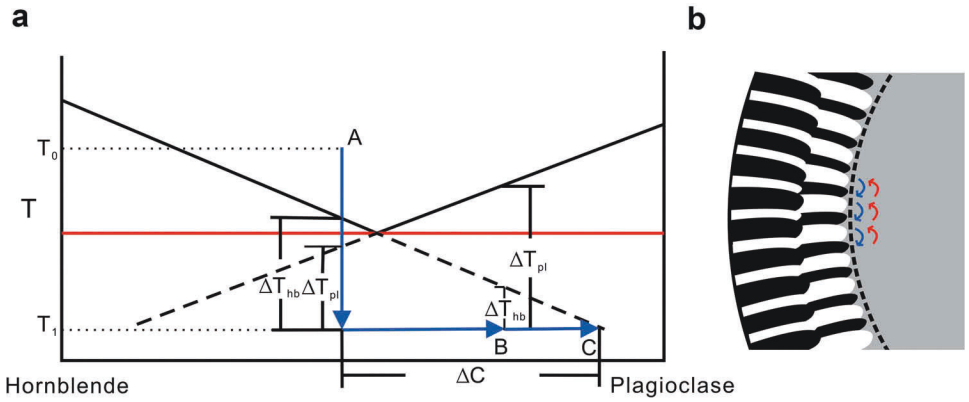


**Figure 12.** (a) A schematic hornblende-plagioclase binary phase diagram showing how disequilibrium crystallization (undercooling) can cause oscillatory banding in the orbicules. For an undercooled off-eutectic liquid of composition *A*, hornblende supersaturation ($\Delta T_{hb}$) will initially be greater than plagioclase supersaturation ($\Delta T_{pl}$), forcing preferential crystallization of hornblende and the generation of a hornblende-rich layer. If crystallization is rapid, the fluid in front of the growing crystal front will become depleted in hornblende component and enriched in plagioclase component (composition of fluid in boundary layer evolves from *A* to *B* to *C*), eventually driving the fluid to preferentially crystallize plagioclase. Once plagioclase is crystallized, further undercooling drives the liquid back to hornblende-enrichment, resulting in the process repeating. The width of each band is controlled by the rate of undercooling, which decreases inward. (b) An example of one band, where both hornblende and plagioclase crystallize, but the ratio is controlled by relative supersaturation. Arrows show direction of secondary diffusion within the fluid.

intersection of the liquidus and solidus represents the eutectic. Extrapolation of the liquidus lines (dashed) for each mineral phase to temperatures below the eutectic represents metastable extensions.

We can consider an orbicule with an initial bulk chemical composition A to the left of the eutectic (Figure 12(a)). Let A cool from an initial temperature $T_0$ to a temperature $T_1$ below the eutectic. At $T_1$, hornblende composition of the melt at saturation (metastable) is defined by point C, which lies at the intersection of the horizontal line $T$-$T_1$ and the metastable liquidus of hornblende. Therefore, the $\Delta C$ marked in Figure 12(a) represents the difference between bulk hornblende concentration and its saturation at $T_1$. $\Delta C$ can be approximated by dividing the undercooling degree ($\Delta T$) by the slope of the liquidus of hornblende ($dT/dC$), that is, $\Delta C = \Delta T/(dT/dC)$, with $\Delta T$ is bounded from our thermal models. The only unknown parameter is the slope of the liquidus of hornblende in the hornblende-plagioclase binary phase diagram. We approximated the slope with that of the liquidus of diopside in the diopside-anorthite binary phase diagram, corresponding to 2.8°C/% (Osborn 1942) or a $\Delta C$ of ~0.7 for an undercooling degree $\Delta T$ of ~200°C. We recognize that this approach in estimating $\Delta C$ is crude, but we are only interested in order of magnitude estimates on growth rates so uncertainties in the above analysis are acceptable. This approach yields growth rates of ~$1.0 \times 10^{-6}$ m/s or ~0.4 cm/hour. The rapid growth rates estimated above by diffusion-controlled growth models are consistent with that bounded independently by our above thermal modelling.

## *On the origin of plagioclase-hornblende oscillatory banding*

The kinetic model above can now help us qualitatively understand how hornblende-rich and plagioclase-rich doublet bands originate (Figure 12(b)). We can approximate crystallization in this system via a binary eutectic. If the original melt composition is slightly off eutectic, disequilibrium crystallization can lead to preferential crystallization of one phase over the other, that is, crystallizing in proportions that exceed that defined by equilibrium crystallization stoichiometry. This concept is illustrated with the binary phase diagram in Figure 12(a), following Porter *et al*. (2009). A similar approach was taken by London (2014).

A melt with an initial bulk chemical composition A that is slightly off-eutectic (towards the hornblende-rich side) cools from an initial temperature $T_0$ to a temperature $T_1$ below the eutectic. If cooling is faster than crystallization can occur, the system would be considered to have undercooled and thus be supersaturated in all of the crystallizing phases. The degree of supersaturation for a particular phase will scale with the degree of undercooling, which can be approximated by the difference between the temperature of the liquid $T_1$ and the temperature of the liquidus line (or metastable extensions of the liquidus) for each phase at bulk composition A. For the bulk composition considered,

supersaturation at $T_1$ is given by $\Delta T_{hb}$ and is greater than that of plagioclase $\Delta T_{pl}$. Plagioclase and hornblende will both crystallize, but the driving force for hornblende is greater and thus would promote an excess of hornblende crystallization compared to plagioclase. However, excess hornblende crystallization will drive the residual melt within the crystallizing boundary layer to become more enriched in plagioclase component and depleted in hornblende component, causing the residual melt to migrate towards the plagioclase-rich end-member (point B). When the degree of plagioclase supersaturation exceeds that of hornblende supersaturation, the residual melt preferentially crystallizes plagioclase. Further cooling causes the local system to switch back to hornblende over-saturation, repeating the sequence and thereby generating oscillating mafic-felsic doublets. Key to this process operating is that diffusion timescales of essential nutrients (e.g. Al (Acosta-Vigil *et al*. 2003)) are comparable to timescales of crystal growth and cooling. If cooling rates are too fast relative to chemical diffusion, the system will quench homogeneously with insufficient time to generate any boundary layer effects. If cooling rates are too slow, then crystallization will occur near equilibrium, preventing the build-up of chemical boundary layers.

## Conclusions, caveats and implications

Compositional and textural mapping of magmatic orbicules from Australia and California (USA) show that the orbicules are composed of concentric bands of alternating mafic and felsic layers. Band widths increase, crystal number densities decrease, and grain size coarsens inward from the rim, but at scales greater than one band, the orbicules show no radial compositional zonation. These observations are consistent with orbicules forming by quenching, perhaps through the injection of hot dioritic liquids into a cooler granitic magma host. We estimated cooling timescales based on a conductive cooling model, bounding crystal growth rates to be at least ~$10^{-6}$ m/s or ~0.4 cm/hr. We showed that the oscillatory banding is controlled by disequilibrium crystallization, wherein hornblende preferentially crystallizes, resulting in the diffusive growth of a chemical boundary layer enriched in plagioclase component, which in turn causes preferential plagioclase crystallization. We also developed a method for obtaining the effective chemical diffusivity of crystal-forming nutrients, arriving at ~$10^{-8}$ $m^2$/s, which is many orders of magnitude greater than diffusivities in silicate melts, but similar to that in water at elevated temperature. We suggest that high effective diffusivities reflect transport through fluids and/or require a strong advective component. These high effective diffusivities in dynamic fluid-rich systems lead to rapid crystal growth. Our work may have implications for the growth of large, metre-scale crystals in other fluid-dominated systems. Pegmatites represent the residual liquids formed after extremely late stage crystallization of a magma, resulting in extreme enrichment of incompatibles like Li, B, and $H_2O$ (London 2008). This enrichment of $H_2O$ may lead to a large amount fluid exsolution through which structurally essential elements and 'nutrients' can be transported through growth media to lead to rapid crystal growth. Finally, we acknowledge that our conclusions are based on the validity of our textural interpretations, which may not be unique. Our interpretations and hypotheses can be tested by future studies.

## Acknowledgments

We thank Ming Tang, Xu Chu, Chenguang Sun, Hehe Jiang, Patrick Phelps and Eytan Sharton-Bierig for useful discussions. Ben Clausen, Chris Ballhaus, David London, and Calvin Barnes are thanked for reviews or editorial comments although this does not necessarily mean that they all agree with the interpretations.

## Disclosure Statement

No potential conflict of interest was reported by the authors.

## Funding

This work was supported by the National Science Foundation [EAR 1753599].

## References

Acosta-Vigil, A. et al., 2003, Solubility of excess alumina in hydrous granitic melts in equilibrium with peraluminous minerals at 700–800 C and 200 MPa, and applications of the aluminum saturation index: Contributions to Mineralogy and Petrology, v. 146, no. 1, p. 100–119. doi:10.1007/s00410-003-0486-6

Baker, D.R., and Hélène, B., 1994, The combined effect of F and H 2 O on interdiffusion between peralkaline dacitic and rhyolitic melts: Contributions to Mineralogy and Petrology, v. 117, no. 2, p. 203–214. doi:10.1007/BF00286843

Ballhaus, C. et al., 2015, Spheroidal textures in igneous rocks–textural consequences of H2O saturation in basaltic melts: Geochimica et cosmochimica acta, v. 167, p. 241–252. doi:10.1016/j.gca.2015.07.029

Berger, B. R. (2014). Petrology and chemistry of the green acres gabbro complex near winchester, riverside county, california. Geological Society Of America Memoirs, 211, 365–394

Bevan, J.C., and Bevan, A.W.R., 2009, Nature and origin of the orbicular granodiorite from Boogardie Station, Western Australia: An ornamental stone of monumental proportions: The Australian Gemmologist, v. 23, p. 373–432.

Christensen, J.N., and DePaolo, D.J., 1993, Time scales of large volume silicic magma systems: Sr isotopic systematics of phenocrysts and glass from the Bishop Tuff, Long Valley, California: Contributions to Mineralogy and Petrology, v. 113, no. 1, p. 100–114. doi:10.1007/BF00320834

Costa, A., 2005, Viscosity of high crystal content melts: Dependence on solid fraction: Geophysical Research Letters, v. 32, no. 22. doi:10.1029/2005GL024303

Donaldson, C.H., 1976, An experimental investigation of olivine morphology: Contributions to Mineralogy and Petrology, v. 57, no. 2, p. 187–213. doi:10.1007/BF00405225

Druitt, T.H. et al., 2012, Decadal to monthly timescales of magma transfer and reservoir growth at a caldera volcano: Nature, v. 482, no. 7383, p. 77. doi:10.1038/nature10706

Durant, D.G., and Fowler, A.D., 2002, Origin of reverse zoning in branching orthopyroxene and acicular plagioclase in orbicular diorite: Fisher Lake, California, De Gruyter.

Eriksson, R., Hayashi, M., and Seetharaman, S., 2003, Thermal diffusivity measurements of liquid silicate melts: International Journal of Thermophysics, v. 24, no. 3, p. 785–797. doi:10.1023/A:1024048518617

Farner, M.J., Lee, C.-T.A., and Putirka, K.D., 2014, Mafic–felsic magma mixing limited by reactive processes: A case study of biotite-rich rinds on mafic enclaves: Earth and Planetary Science Letters, v. 393, p. 49–59. doi:10.1016/j.epsl.2014.02.040

Fetherston, J.M., 2010, "Dimension stone in Western Australia —Volume 2—Dimension stones of the Southern, Central Western, and Northern Regions." Geological Survey Western Australia, Mineral Res Bulletin 24 (2010): 35-43..

Gao, S. et al., 1998, Chemical composition of the continental crust as revealed by studies in East China: Geochimica et cosmochimica acta, v. 62, no. 11, p. 1959–1975. doi:10.1016/S0016-7037(98)00121-5

Ghiorso, M.S., and Gualda, G.A.R., 2015, An H 2 O–CO 2 mixed fluid saturation model compatible with rhyolite-MELTS: Contributions to Mineralogy and Petrology, v. 169, no. 6, p. 53. doi:10.1007/s00410-015-1141-8

Ginibre, C., Wörner, G., and Kronz, A., 2007, Crystal zoning as an archive for magma evolution: Elements, v. 3, no. 4, p. 261–266. doi:10.2113/gselements.3.4.261

Gualda, G.A.R. et al., 2012a, Rhyolite-MELTS: A modified calibration of MELTS optimized for silica-rich, fluid-bearing magmatic systems: Journal of Petrology, v. 53, no. 5, p. 875–890. doi:10.1093/petrology/egr080

Gualda, G.A.R. et al., 2012b, Timescales of quartz crystallization and the longevity of the Bishop giant magma body: PloS One, v. 7, no. 5, p. e37492. doi:10.1371/journal.pone.0037492

Hartlieb, P. et al., 2016, Thermo-physical properties of selected hard rocks and their relation to microwave-assisted comminution: Minerals Engineering, v. 91, p. 34–41. doi:10.1016/j.mineng.2015.11.008

Huang, R., and Andreas, A., 2012, The titanium-in-quartz (TitaniQ) thermobarometer: A critical examination and re-calibration: Geochimica et cosmochimica acta, v. 84, p. 75–89. doi:10.1016/j.gca.2012.01.009

Hurwitz, S., and Navon, O., 1994, Bubble nucleation in rhyolitic melts: Experiments at high pressure, temperature, and water content: Earth and Planetary Science Letters, v. 122, no. 3–4, p. 267–280. doi:10.1016/0012-821X(94)90001-9

Jahns, R.H., and Wayne Burnham, C., 1958, Experimental studies of pegmatite genesis: Melting and crystallization of granite and pegmatite: US Geological Survey Bulletin, v. 69, p. 1592–1593.

Kemp, A.I.S., and Hawkesworth, C.J., 2005, Generation and secular evolution of the continental crust: The Crust, v. 3, p. 349.

Klug, C., and Cashman, K.V., 1996, Permeability development in vesiculating magmas: Implications for fragmentation: Bulletin of Volcanology, v. 58, no. 2–3, p. 87–100. doi:10.1007/s004450050128

Lange, R.A., Cashman, K.V., and Navrotsky, A., 1994, Direct measurements of latent heat during crystallization and melting of a ugandite and an olivine basalt: Contributions to Mineralogy and Petrology, v. 118, no. 2, p. 169–181. doi:10.1007/BF01052867

Lasaga, A.C., 2014, Kinetic theory in the earth sciences: Princeton university press. Princeton, New Jersey.

Lee, C.-T.A. et al., 2015, Field and model constraints on silicic melt segregation by compaction/hindered settling: The role of water and its effect on latent heat release: American Mineralogist, v. 100, no. 8–9, p. 1762–1777. doi:10.2138/am-2015-5121

Lewis, A. et al., 2015, Industrial crystallization: Fundamentals and applications. Cambridge: Cambridge University Press.

Li, Y.-H., and Gregory, S., 1974, Diffusion of ions in sea water and in deep-sea sediments: Geochimica et cosmochimica acta, v. 38, no. 5, p. 703–714. doi:10.1016/0016-7037(74)90145-8

Liao, K.Z., Morton, D.M., and Lee, C.-T.A., 2013, Geochemical diagnostics of metasedimentary dark enclaves: A case study from the Peninsular Ranges Batholith, southern California: International Geology Review, v. 55, no. 9, p. 1049–1072. doi:10.1080/00206814.2012.753684

Lofgren, G., 1974a, An experimental study of plagioclase crystal morphology; isothermal crystallization: American Journal of Science, v. 274, no. 3, p. 243–273. doi:10.2475/ajs.274.3.243

Lofgren, G.E., 1974b, Temperature induced zoning in synthetic plagioclase feldspar: The feldspars, p. 362–377.

London, D., 2008, Pegmatites: Can. Mineral., v. 10, p. 347.

London, D., 2014, Subsolidus isothermal fractional crystallization: American Mineralogist, v. 99, no. 2–3, p. 543–546. doi:10.2138/am.2014.4693

McCarthy, A. et al., 2016, Melt extraction zones in shallow arc plutons: Insights from Fisher Lake orbicules (Sierra Nevada, Western USA): Journal of Petrology, v. 57, no. 10, p. 2011–2052. doi:10.1093/petrology/egw068

McCarthy, A., and Othmar, M., 2017, Mineral growth in melt conduits as a mechanism for igneous layering in shallow arc plutons: Mineral chemistry of Fisher Lake orbicules and comb layers (Sierra Nevada, USA): Contributions to Mineralogy and Petrology, v. 172, no. 7, p. 55. doi:10.1007/s00410-017-1371-z

Moitra, P., and Gonnermann, H.M., 2015, Effects of crystal shape- and size-modality on magma rheology: Geochemistry, Geophysics, Geosystems, v. 16, no. 1, p. 1–26. doi:10.1002/2014GC005554

Moore, J.G., and Lockwood, J.P., 1973, Origin of comb layering and orbicular structure, Sierra Nevada batholith, California: Geological Society of America Bulletin, v. 84, no. 1, p. 1–20. doi:10.1130/0016-7606(1973)84<1:OOCLAO>2.0.CO;2

Morgan, G.B., Acosta-Vigil, A., and London, D., 2008, Diffusive equilibration between hydrous metaluminous-peraluminous haplogranite liquid couples at 200 MPa (H 2 O) and alkali transport in granitic liquids: Contributions to Mineralogy and Petrology, v. 155, no. 2, p. 257–269. doi:10.1007/s00410-007-0242-4

Neilson, G.F., and Weinberg, M.C., 1979, A test of classical nucleation theory: Crystal nucleation of lithium disilicate glass: Journal of Non-crystalline Solids, v. 34, no. 1, p. 137–147. doi:10.1016/0022-3093(79)90013-9

Nigrini, A., 1970, Diffusion in rock alteration systems; I, Prediction of limiting equivalent ionic conductances at elevated temperatures: American Journal of Science, v. 269, no. 1, p. 65–91. doi:10.2475/ajs.269.1.65

Osborn, E.F., 1942, The system CaSiO 3-diopside-anorthite: American Journal of Science, v. 240, no. 11, p. 751–788. doi:10.2475/ajs.240.11.751

Porter, D.A., Easterling, K.E., and Sherif, M., 2009, Phase transformations in metals and alloys, (Revised reprint). Boca Raton:CRC press.

Raymond, O.L. et al., 2012, Surface geology of Australia 1: 1 million scale data set 2012 edition. Commonwealth of Australia (Geoscience Australia), Canberra, Australia.

Reid, M.R. et al., 1997, Prolonged residence times for the youngest rhyolites associated with Long Valley Caldera: 230Th—238U ion microprobe dating of young zircons: Earth and Planetary Science Letters, v. 150, no. 1–2, p. 27–39. doi:10.1016/S0012-821X(97)00077-0

Shea, T. et al., 2015a, Accuracy of timescales retrieved from diffusion modeling in olivine: A 3D perspective: American Mineralogist, v. 100, no. 10, p. 2026–2042. doi:10.2138/am-2015-5163

Shea, T., Lynn, K.J., and Garcia, M.O., 2015b, Cracking the olivine zoning code: Distinguishing between crystal growth and diffusion: Geology, v. 43, no. 10, p. 935–938. doi:10.1130/G37082.1

Smillie, R.W., and Turnbull, R.E., 2014, Field and petrographical insight into the formation of orbicular granitoids from the Bonney Pluton, southern Victoria Land, Antarctica: Geological Magazine, v. 151, no. 3, p. 534–549. doi:10.1017/S0016756813000484

Somerton, W.H., 1992, Thermal properties and temperature-related behavior of rock/fluid systems, Volume 37. Amsterdam: Elsevier.

Sparks, R.S.J., 2003, Dynamics of magma degassing: Geological Society, London, Special Publications, v. 213, no. 1, p. 5–22. doi:10.1144/GSL.SP.2003.213.01.02

Swanson, S.E., 1977, Relation of nucleation and crystal-growth rate to the development of granitic textures: American Mineralogist, v. 62, no. 9–10. p. 966–978.

Sylvester, A.G., 2011, The nature and polygenetic origin of orbicular granodiorite in the Lower Castle Creek pluton, northern Sierra Nevada batholith, California: Geosphere, v. 7, no. 5, p. 1134–1142. doi:10.1130/GES00664.1

Vance, D., and O'nions, R.K., 1990, Isotopic chronometry of zoned garnets: Growth kinetics and metamorphic histories: Earth and Planetary Science Letters, v. 97, no. 3–4, p. 227–240. doi:10.1016/0012-821X(90)90044-X

Watson, E.B., and Thomas, M., 2009, Non-equilibrium isotopic and elemental fractionation during diffusion-controlled crystal growth under static and dynamic conditions: Chemical Geology, v. 267, no. 3–4, p. 111–124. doi:10.1016/j.chemgeo.2008.10.036

Wiebe, R.A., 1994, Silicic magma chambers as traps for basaltic magmas: The Cadillac Mountain intrusive complex, Mount Desert Island, Maine: The Journal of Geology, v. 102, no. 4, p. 423–437. doi:10.1086/629684

# Appendix

## Analytical methods

Six Australian orbicule samples (AUS-1, AUS-2, AUS-12, AUS-15, AUS-16, AUS-17) and one California sample (CA-1) were scanned with a micro-XRF element mapper (Horiba XGT 7000) at Rice University. Each sample was scanned for ~2 h using a 400 $\mu m$ spot size with a 50 kV beam. Results were processed by ImageJ. The major element maps of hornblendes in the different doublet bands were done by wavelength dispersive electron probe microanalyzer (EPMA) at Rice University. Si, Al, Fe, Mg, Ca, K, Na, and Ti were mapped for one hornblende grain in each doublet band (rim, mid, core; Figure 7) with a voltage 15 kV, current of ~50 nA, and dwell times of 10 ms.

## Numerical models

Equation (1) is non-dimensionalized as $r^* = \frac{r}{R^*}, t^* = \frac{t}{\tau}$, and $T^* = \frac{T-T_\infty}{\Delta T}$, where $\Delta T = T_0 - T_\infty$, resulting in

$$\frac{\partial T^*}{\partial t^*} = \frac{2k\tau}{R^{*2}}\frac{1}{r^*}\frac{\partial T^*}{\partial r^*} + \frac{k\tau}{R^{*2}}\frac{\partial^2 T^*}{\partial r^{*2}} + \frac{L}{C_p\Delta T}\frac{dF}{dT^*}\frac{\partial T^*}{\partial t^*} \tag{A1}$$

Letting $\tau = \frac{R^{*2}}{k}$ yields

$$\frac{\partial T^*}{\partial t^*} = \frac{2}{r^*}\frac{\partial T^*}{\partial r^*} + \frac{\partial^2 T^*}{\partial r^{*2}} + \frac{L}{C_p\Delta T}\frac{dF}{dT^*}\frac{\partial T^*}{\partial t^*} \tag{A2}$$

The discrete form of equation A2 using finite element differences is

$$\left(1 - \frac{L}{C_p\Delta T}\frac{dF}{dT^*}\right)\frac{T_n^{i+1} - T_n^i}{\Delta t} = \frac{1}{r^*}\frac{T_{n+1}^i - T_{n-1}^i}{\Delta r} + \frac{T_{n+1}^i - 2T_n^i + T_{n-1}^i}{(\Delta r)^2} \tag{A3}$$

where the superscript on T represents time and the subscript denotes the spatial grid. $\Delta t$ is the time step and $\Delta r$ denotes the spatial interval. Rewriting Equation (A3) using the implicit method, we obtain

$$\left(1 - \frac{L}{C_p\Delta T}\frac{dF}{dT^*}\right)\frac{T_n^{i+1} - T_n^i}{\Delta t} = \frac{1}{(n-1)\Delta r}\frac{T_{n+1}^{i+1} - T_{n-1}^{i+1}}{\Delta r} + \frac{T_{n+1}^{i+1} - 2T_n^{i+1} + T_{n-1}^{i+1}}{(\Delta r)^2} \tag{A4}$$

which can be rearranged to yield

$$T_n^i = -\frac{n-2}{n-1}\beta T_{n-1}^{i+1} + (2\beta+1)T_n^{i+1} - \frac{n}{n-1}\beta T_{n+1}^{i+1} \tag{A5}$$

where $\boldsymbol{\beta} = \frac{\boldsymbol{\Delta t}}{(\boldsymbol{\Delta r})^2} / \left(1 - \frac{\boldsymbol{L}}{\boldsymbol{C_p\Delta T}}\frac{\boldsymbol{dF}}{\boldsymbol{dT^*}}\right)$. In this case, $\beta$ is not a constant and it changes with $\frac{dF}{dT^*}$. $\frac{dF}{dT^*}$ reflects how fast crystal fraction changes with temperature. To solve for $\frac{dF}{dT^*}$, we used the thermodynamic program MELTS (Gualda *et al*. 2012a; Ghiorso and Gualda 2015) to generate a parameterization for crystal fraction ($F$) as a function of temperature ($T$). A model bulk chemical composition of dioritic orbicules was chosen (Gao *et al*. 1998) and representative granite (Kemp and Hawkesworth 2005); since we are interested in order of magnitude constraints, generalized values are adopted. The chosen compositions may be different from our samples but the exact composition is not critical for our parameterizations, given uncertainties in thermal models. We assumed a bulk closed system water content of 4 wt% for *F(T)* calculations. Detailed equilibrium crystallization diagrams for both diorite and granite can be obtained by running P-T sequences in the MELTS for the estimated bulk chemical compositions at ~0.03 GPa, corresponding to ~1 km depth. The exact pressure is also not important as we are only interested in understanding the general behaviour of *F* versus *T* (Figure 9(b)). The MELTS results show that the liquidus for diorite and granite is 1095°C and 936°C, and solidus for diorite is 720°C and 679°C for granite.